Nanoscale

Metallic 2D Janus SNbSe Layers Driven by a Structural Phase Change

Journal:	*Nanoscale*
Manuscript ID	NR-ART-10-2024-004059.R1
Article Type:	Paper
Date Submitted by the Author:	24-Dec-2024
Complete List of Authors:	Wu, Cheng Lun; Arizona State University, Materials Science and Engineering, School for Engineering of Matter, Transport and Energy Sayyad, Mohammed Y. ; Arizona State University, Materials Science and Engineering, School for Engineering of Matter, Transport and Energy Sailus, Renee ; Arizona State University, Materials Science and Engineering, School for Engineering of Matter, Transport and Energy Dey, Dibyendu ; Arizona State University, Department of Physics; SRM Institute of Science and Technology (Deemed to be University), Department of Physics and Nanotechnology Xie, Jing; Arizona State University, Electrical Computer and Energy Engineering Hays, Patrick ; Arizona State University, Materials Science and Engineering, School for Engineering of Matter, Transport and Energy Kopaczek, Jan ; Arizona State University, Materials Science and Engineering, School for Engineering of Matter, Transport and Energy ; Wroclaw University of Science and Technology Faculty of Fundamental Problems of Technology, Department of Semiconductor Materials Engineering, Faculty of Fundamental Problems of Technology Ou, Yunbo; Arizona State University, Materials Science and Engineering, School for Engineering of Matter, Transport and Energy Susarla, Sandhya ; Arizona State University, Materials Science and Engineering, School for Engineering of Matter, Transport and Energy Esqueda, Ivan; Arizona State University, Electrical Computer and Energy Engineering Botana, Antia ; Arizona State University, Department of Physics Tongay, Seth Ariel; Arizona State University, Materials Science and Engineering, School for Engineering of Matter, Transport and Energy

Metallic 2D Janus SNbSe Layers Driven by a Structural Phase Change

Cheng-Lun Wu[1], Mohammad Y. Sayyad[1], Renee E. Sailus[1], Dibyendu Dey[2,5], Jing Xie[3], Patrick Hays[1], Jan Kopaczek[1,4], Yunbo Ou[1], Sandhya Susarla[1], Ivan S. Esqueda[3], Antia S. Botana[2], Seth A. Tongay[1,]*

[1]*Materials Science and Engineering, School for Engineering of Matter, Transport and Energy, Arizona State University, Tempe, Arizona 85287, USA*

[2]*Department of Physics, Arizona State University, Arizona 85287, USA*

[3]*Electrical Computer and Energy Engineering, Arizona State University, Arizona 85287, USA*

[4]*Department of Semiconductor Materials Engineering, Faculty of Fundamental Problems of Technology, Wroclaw University of Science and Technology, Wybrzeże Wyspiańskiego 27, 50-370 Wrocław, Poland*

[5] *Department of Physics and Nanotechnology, SRM Institute of Science and Technology, Kattankulathur, Tamilnadu 603203, India*

KEYWORDS: Janus, synthesis, microscopy, phononics, transition metal dichalcogenide, NbS_2, $NbSe_2$, SNbSe

ABSTRACT

The discovery of two-dimensional (2D) Janus materials has ignited significant research interest, particularly for their distinct properties diverging from their classical 2D transition metal dichalcogenide (TMD) counterparts. While semiconducting 2D Janus TMDs have been demonstrated, examples of metallic Janus layers are still rather limited. Here, we address this gap by experimentally synthesizing and characterizing metallic Janus layers, focusing on SNbSe and SeNbS, derived from monolayer NbS_2 and $NbSe_2$ using a plasma-assisted technique. Our results show that Nb-based 2D Janus layers form after 1H-to-1T phase transition, marking a phase transition-induced formation of Janus layers. Our comprehensive spectroscopy and microscopy studies, including Z-contrast high angle annular dark field scanning transmission electron microscopy, reveal the phononic and structural properties during Janus SeNbS formation and establish their energetic stability. Density functional theory (DFT) simulations provide insights into the phononic and electronic properties of these materials, shedding light on their potential for diverse applications. Overall, our results demonstrate the realization of niobium-based Janus metals and expand the library of metallic Janus layers.

INTRODUCTION

In the realm of two-dimensional (2D) materials, the emergence of Janus materials has sparked considerable excitement owing to their unique properties that are inherently different from their classical 2D counterparts. 2D Janus materials, characterized by their asymmetry across opposing faces and concurrent colossal polarization fields, offer a diverse array of functionalities with promising applications

in electronics, photonics, and beyond. For example, theoretical studies to date have shown that the mirror symmetry breaking in these materials enables a wealth of exciting properties including but not limited to long-lived excitons,[1] spin-orbit coupling (SOC) induced Rashba splitting,[2-4] large built-in electric fields,[5, 6] and topological phases such as skyrmions.[7-10]

However, the scope of Janus materials has largely been confined to semiconducting transition metal dichalcogenides (TMDs) such as SMoSe and SWSe,[1, 5, 6, 11-18] leaving a significant gap in our understanding of their metallic counterparts. Here, the significance of realizing metallic Janus materials extends beyond the mere expansion of the materials catalog. These materials can facilitate the integration of semiconducting Janus layers into more complex device structures and polarization-engineered 2D superlattices by interfacing them with their metallic counterparts. Furthermore, heterostructures formed by interfacing metallic Janus layers with other classical 2D materials can sustain exotic properties induced by the changes in their sheet carrier density and symmetry breaking.[19, 20] Realizing metallic Janus layers can also pave the way for novel applications in areas such as energy storage,[21, 22] hydrogen evolution reaction,[23] photocatalysis and optoelectronics,[24] and notably, the exploration of ferroelectric phenomena and polarization-driven functionalities as originally predicted by Anderson and Blaunt.[25-30]

While the existence of metallic Janus layers[31-34] has been postulated using first-principles calculations, thus far experimental realization has remained elusive. Among the proposed metallic candidates, SMoH metallic layers stand out, yet their validation through experimental studies remains in its nascent stages.[35-37] Several other theoretically predicted candidates have emerged from the metallic TMD family, including Nb-based NbSSe,[32, 38] Ta-based TaSSe,[39] and Ti-based 1T-TiSSe.[40, 41] In the case of Janus NbSSe, there are only a few studies on that material system mostly limited to theoretical prediction such as on nanoscroll formation,[34] battery application,[42] or just electronic band structure calculations.[32, 38] Notably, our theoretical calculations (SI Table S1 and S2) suggest that trigonal prismatic (1H) Nb-based TMDs exhibit the potential to undergo a structural phase transition to octahedral (1T) coordination, driven by Janus formation. These challenges and opportunities underscore the need for robust experimental investigations to demonstrate and elucidate the properties of metallic Janus layers.

In this study, we demonstrate and establish the structural, phononic, and electronic properties of metallic 2D Janus SNbSe and SeNbS (bottom-middle-top atomic layer) using a plasma-assisted technique.[11, 12] The results show that SNbSe and SeNbS can be stabilized starting from monolayer NbS_2 and $NbSe_2$, respectively. During the transformation from classical to Janus TMD, the host materials undergo a 1H-to-1T phase transformation, representing the first of its kind in Janus layer synthesis that results in 1T-SNbSe and 1T-SeNbS. Comprehensive spectroscopy and microscopy studies successfully capture the phase transition during the 1H-to-1T Janus SNbSe formation and establish the structural properties through Z-contrast high-angle annular dark field (HAADF) scanning transmission electron microscopy (STEM). Density functional theory (DFT) simulations elucidate the 1H-to-1T phase transition and offer insights into phononic properties while establishing their electronic properties together with four-probe transport measurements.

RESULTS

Synthesis of parent classical TMDs

Monolayer 1H-NbS_2 (Figure 1a) were grown on single-side-polished *c*-cut sapphire substrates using a well-established ambient pressure chemical vapor deposition (APCVD) method (Figure 1b).[43] This APCVD growth method typically yields monolayer and few-layer NbS_2 domains with lateral dimensions ranging from 1 to 10 μm, distributed across 1 x 1.5 cm^2 sapphire substrates. The domains grown are typically triangular and hexagonal, but slight distortion in the flake shape could occur due to lattice mismatch between the sapphire substrate and NbS_2 crystal.[44] In contrast, due to the inherent defects and poor crystalline quality of CVD-grown $NbSe_2$, high-quality monolayer $NbSe_2$ sheets were directly exfoliated from bulk chemical vapor transport (CVT) $NbSe_2$ crystals[45] using a viscoelastic exfoliation technique[46] (Figure 1c). Optical microscope images of the monolayers (Figure 1b-c) reveal the size and morphology, while semi-contact atomic force microscopy (AFM) (NT-MDT) was used to quantify the thickness of the monolayer, confirming values of ~0.9 nm for NbS_2 and ~1.5 nm for $NbSe_2$ (Figure 1d-e). The slight deviation from the theoretical value of monolayer $NbSe_2$ (~1.1 nm)[47] is likely attributed to an interfacial gap between the film and substrate during the substrate during the exfoliation and stamping process. This gap can be flattened by contact mode AFM scan or annealing at 200 ˚C under ultra-high vacuum.

Raman spectroscopy was used to further verify the growth and thickness of NbS_2 and $NbSe_2$ by examining the out-of-plane A_2" and in-plane E' vibrational modes, which represent the most prominent peaks for these crystal systems, as shown in Figure 1f-g. As reported in previous studies, the Raman spectra of both NbS_2 and $NbSe_2$ exhibit a strong dependence on the layer thickness.[44, 48-50] The vibrational modes of NbS_2, particularly A_2" mode, display a pronounced dependence on thickness due to interlayer interactions and dielectric screening of the long-range Coulomb interactions.[50] This is demonstrated by the blue shift of A_2" from ~377 cm^{-1} in monolayer NbS_2 to ~383 cm^{-1} in the few-layer form.[48, 50] For $NbSe_2$, the characteristic out-of-plane A_{1g} and in-plane E_{2g} modes exhibit similar thickness-dependent shifts, with the A_{1g} mode red-shifting from ~230 cm^{-1} in the 4-layer structure to ~227 cm^{-1} in the monolayer, while E_{2g} mode blue-shifts from ~240 cm^{-1} to ~243 cm^{-1} with decreasing thickness.[49] The sharp peaks at ~418 cm^{-1} arise from the *c*-cut sapphire substrate used for NbS_2 APCVD growth. Additionally, a broad peak at around 180 cm^{-1} in the monolayer $NbSe_2$ spectra is attributed to a soft phonon mode, likely attributed to the charge density wave (CDW) phase.[51]

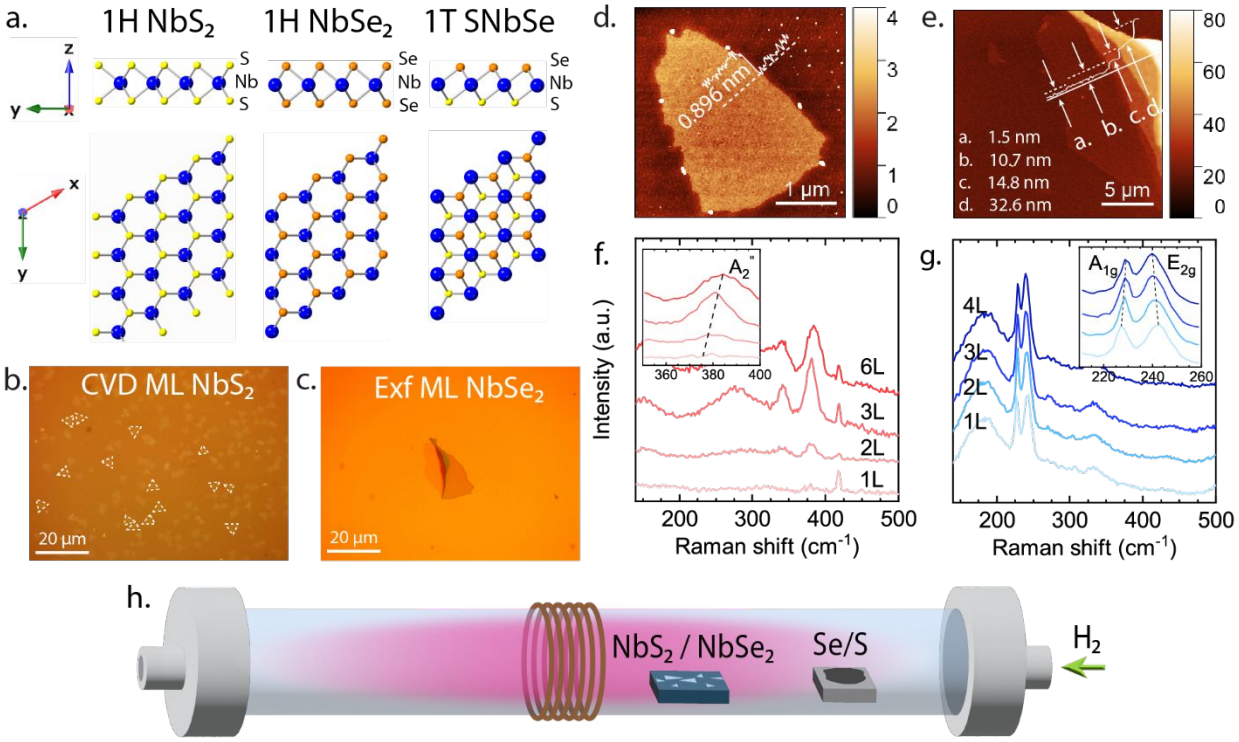

Figure 1. (a) Top-down and cross-sectional atomic structure of monolayer 1H-NbS_2, 1H-$NbSe_2$, and 1T-SNbSe. (b)-(c) optical microscope images of APCVD grown monolayer and few-layer NbS_2 and exfoliated $NbSe_2$, respectively. (d)-(e) AFM topography scans of monolayer NbS_2 and $NbSe_2$ corresponding to the domains shown in (b) and (c). (f)-(g) Layer-dependent Raman spectra for few-layer to monolayer APCVD grown NbS_2 and exfoliated CVT grown $NbSe_2$, respectively. (h) Schematic of the room temperature SEAR Janus conversion setup, depicting an inductively coupled hydrogen plasma (pink illumination), and both the TMD sample and the chalcogen source placed upstream of the copper coil.

SEAR sulfurization and selenization processes

Monolayer NbS_2 and $NbSe_2$ were converted into their Janus counterparts, SNbSe and SeNbS (Figure 1a), using room temperature selective epitaxial atomic replacement (SEAR) plasma process (Figure 1h).[5, 11, 12, 52, 53] SEAR selenization and sulfurization processes were conducted within a one-inch diameter quartz tube reactor, as illustrated in Figure 1h, where monolayer NbS_2 ($NbSe_2$) on substrate were positioned downstream from the solid chalcogen source. The SEAR Janus conversion process for Nb-based TMDs is similar to that used for SWSe and SMoSe material systems[11, 12], employing RF power at 13.56 MHz frequency to generate hydrogen inductively coupled plasma (ICP), facilitating the atomic replacement reaction.

The process begins with the creation of chalcogen vacancies in the topmost atomic layer of the TMD via etching by H^+ ions and H radicals produced by H_2 ICP. The H radicals initially adsorb onto the top chalcogen atoms, forming a weakly-bonded intermediate species. Subsequently, the energized H^+ ions

break the bond between the transition metal and the intermediate chalcogen species to create a chalcogen vacancy. Simultaneously, the chalcogen source (S or Se) positioned upstream is dissociated by H_2 plasma to form H_2S or H_2Se vapor, which is carried downstream to the vacancy sites by gas flow. The vacancies are subsequently filled by a new chalcogen species as the H_2S (H_2Se) vapor is dissociated again by H_2 plasma into elemental S/Se and H radicals, completing the chalcogen substitution. This plasma-driven process enables controlled chalcogen replacement without requirements for thermal assistance, creating a Janus structure from the parent TMD structure.[11, 12, 52] More detailed descriptions of the SEAR method and process parameters used in this work are provided in the Supplementary Information file.

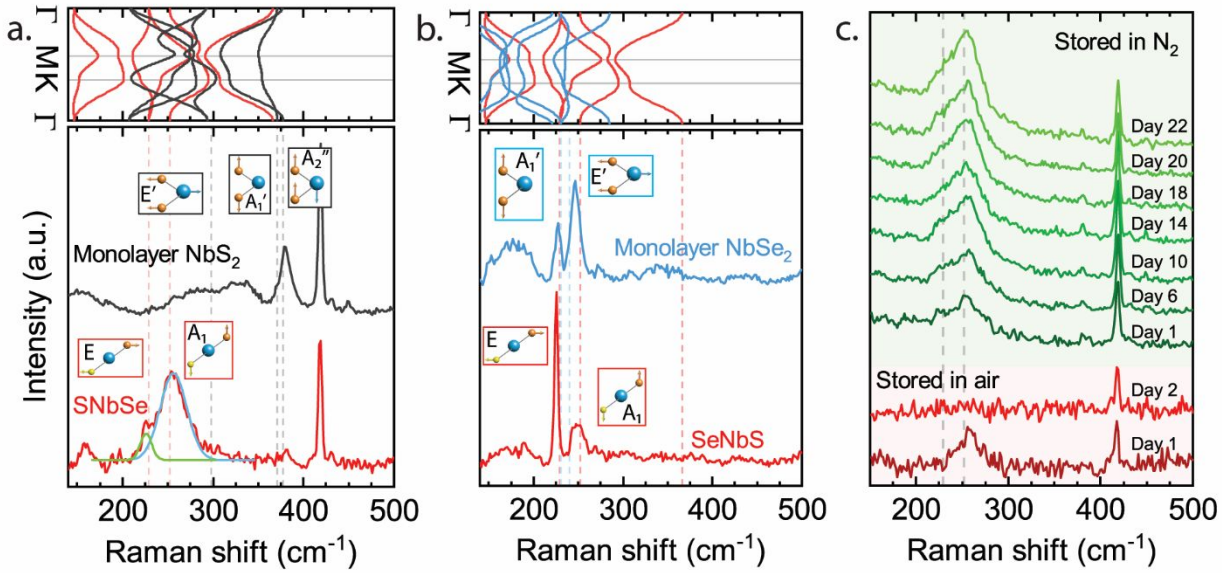

Figure 2. Raman spectra for (a) Technically CVD-grown monolayer NbS_2 and SEAR selenized SNbSe, displaying the characteristic vibrational modes of E", E', A_1', and A_2" for NbS_2 and E (fitted in green) and A_1 (fitted in blue) modes for SNbSe. Above the Raman spectra align the corresponding DFT-calculated phonon dispersion for both materials in their respective colors. (b) Exfoliated monolayer $NbSe_2$ and SEAR sulfurized SeNbS, displaying A_1' and E' for $NbSe_2$, and E and A_1 for SeNbS. The corresponding phonon dispersion is also aligned above the Raman spectra. The quality of the CVD-grown monolayer is inferior to that of the CVT-grown and exfoliated $NbSe_2$, which affects the sharpness and FWHM of the Raman peaks. (c) Stability study of SEAR selenized SNbSe when stored in ambient conditions (red) and an inert N_2-filled glovebox (green).

Notably, both 1H-NbS_2 and 1H-$NbSe_2$ parent TMDs undergo a 1H-to-1T structural transformation after the SEAR conversion to Janus SNbSe and SeNbS, respectively. The driving mechanism of the 1H-to-1T transition is believed to originate from the non-equilibrium thermodynamic H_2 plasma process during the SEAR conversion, which provides sufficient kinetic energy to initiate an in-plane displacement/slide in the top-chalcogen layer as the S vacancies are replaced by Se atoms, resulting in the formation of an energetically favorable 1T phase. Moreover, the presence of S vacancies (atomic sites not filled by Se atoms during the conversion process) further stabilizes the 1T phase. Similar 1H-to-1T phase transitions were

previously observed for monolayer MoS_2 and $MoTe_2$, induced by low-energy Ar and H_2 plasma treatment, respectively, while preserving the top chalcogen layer without etching.[54, 55] Conversely, in the SEAR Janus process, H_2 plasma with a high enough energy to break the S-Nb bond is applied to disrupt the top chalcogen layer and the newly attached Se atom experiences the in-plane shift when settling in the vacancy sites and bonding to Nb. This phase transition is captured using ex-situ Raman spectroscopy, which provides insight into the distinct vibrational modes, as shown in Figure 2, with more direct measurements discussed later (see Figure 4).

Post-conversion, the Raman spectra of both Janus SNbSe and SeNbS exhibit notable shifts, with both structures displaying a prominent out-of-plane A_1 peak at ~254 cm^{-1} and an in-plane E peak at ~224 cm^{-1} (Figure 2a-b). These experimental results align relatively well with the Raman-active vibrational modes and the peak positions predicted by density functional theory (DFT) simulations for the 1T-phase Janus structures (see SI Figure S1). In the case of 1H-NbS_2 to 1T-SNbSe transformation, the transition is marked by the disappearance of the NbS_2 A_{1g} peak at ~377 cm^{-1} and the emergence of A_1 and E Janus SNbSe peaks at ~254 cm^{-1} and ~224 cm^{-1}, respectively. Conversely, the 1H $NbSe_2$ to 1T SeNbS transition is observed through the red-shifting of the $NbSe_2$ E' mode from ~242 cm^{-1} to the SeNbS E mode ~224 cm^{-1}, and the blue-shifting of the $NbSe_2$ A_1' mode from ~227 cm^{-1} to the SeNbS A_1 mode at ~251 cm^{-1}. The disappearance of the unique parent NbS_2 and $NbSe_2$ A and E Raman modes serves as an indication that both materials were fully converted into their Janus counterparts. It is worth noting that, although the peak positions agree well with calculated phonon dispersions, the relative intensities between A_1 and E peaks for SNbSe and SeNbS are opposite from each other, i.e., the A_1 mode is stronger than E mode in SNbSe, while the E mode is stronger than A_1 mode in SeNbS. We observe the same relative intensities between the in-plane and out-of-plane modes in their respective parent TMD Raman spectra, indicating that the relationship is preserved after Janus conversion, and the change in the polarizability is different in Janus structure compared to TMD.

Additionally, changes in the full width at half maximum (FWHM) of SNbSe and SeNbS peaks were also observed following each conversion. Specifically, the FWHM of CVD-grown monolayer NbS_2 A_{1g} peak (~13 cm^{-1}) exhibited a substantial broadening after converted to SNbSe (A_1~27 cm^{-1}), compared to the FWHM of monolayer exfoliated from CVT $NbSe_2$ (A_1'~7 cm^{-1}, E'~13 cm^{-1}) and its subsequent Janus derivative SeNbS (A_1~15 cm^{-1}, E~4 cm^{-1}). These differences are likely attributed to lower crystallinity and increased defect density in the monolayers grown by CVD, compared to monolayers exfoliated from high-quality CVT bulk crystals. Furthermore, the Raman signal from monolayer SNbSe gradually decreases by laser exposure while collecting spectra (SI Figure S2). The areas from which the Raman signal was measured revealed increased surface roughening and, as mentioned above, decreased Raman intensity (see AFM scan and Raman maps SI Figure S3). Moreover, spot-like discolorations were observed using an optical microscope (SI Figure S4). Such behaviors were previously reported for ultrathin $NbSe_2$, attributing to laser-induced oxidation.[56] Our findings suggest that this effect is exacerbated following the plasma SEAR conversion of parent NbS_2 and $NbSe_2$ TMDs into their Janus forms. The laser-induced deterioration highlights the increased vulnerability of Janus SNbSe and SeNbS structures.

The environmental stability of a freshly converted SNbSe was assessed by comparing the storage condition, namely, in an ambient condition or N_2-filled glovebox, and monitoring its Raman intensity over an extended period. Exposure to an ambient condition for 24 hours resulted in the complete disappearance of all characteristic Raman modes of monolayer SNbSe, as shown in the bottom part (red) of Figure 2c. This degradation is likely attributed to the oxidation of SNbSe, consistent with the previously reported oxidation behavior of ultra-thin NbS_2.[44] Additionally, the optical microscopy images (SI Figure S5) captured the reduced flake visibility, further aligning with prior observations in NbS_2.[44] In contrast, when stored inside a controlled N_2-filled glovebox ($O_2 < 0.01$ ppm, and $H_2O < 0.01$ ppm), the monolayer SNbSe remained stable and visible for more than 20 days, as evident by the unchanged Raman modes shown in the top part (green) of Figure 2c. Each time, all the Raman spectra were collected from several different monolayers and the signal was averaged. Therefore, the absence of oxygen and/or humidity effectively mitigated oxidation of the surface Se layer over a long period, reinforcing the hypothesis of oxidation-driven degradation in SNbSe under ambient conditions.

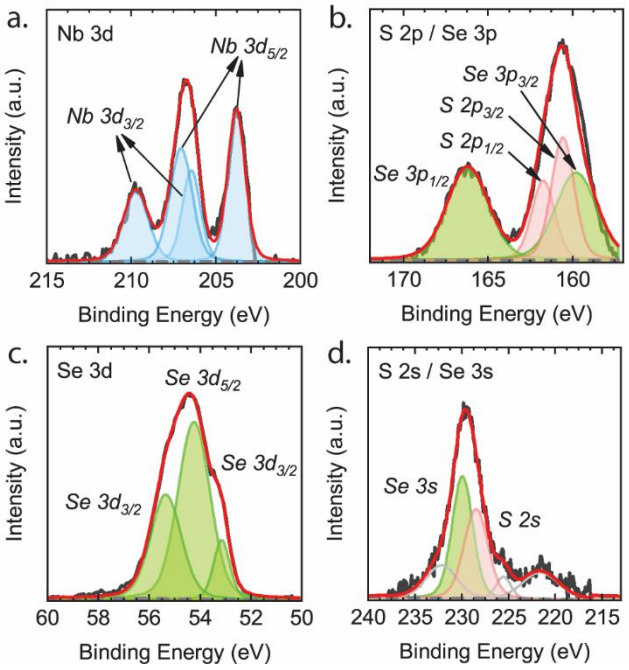

Figure 3. XPS analysis for Janus SNbSe converted from CVD-grown NbS_2 using room-temperature SEAR plasma selenization. The collected spectra are deconvoluted to show the orbital contributions for (a) Nb $3d_{3/2}$ and Nb $3d_{5/2}$, (b) Se $3p_{1/2}$, S $2p_{3/2}$, S $2p_{1/2}$, and Se $3p_{3/2}$, (c) Se $3d_{3/2}$ and Se $3d_{5/2}$, and (d) Se 3s and S 2s. The presence of both S and Se signals indicates the bonding of Nb-S and Nb-Se in the Janus structure.

Elemental analysis and understanding of Janus SNbSe

Compositional analysis of pristine 1T-SNbSe, synthesized through selenization of APCVD-grown NbS_2, was conducted using X-ray photoelectron spectroscopy (XPS) (Kratos Axis Supra+). The survey scan (SI Figure S6) confirmed the presence of Nb, Se, and S in the Janus structure. The XPS spectrum for Nb 3d (Figure 3a) was well-resolved, revealing the characteristic peaks for Nb $3d_{3/2}$ (at 209.7 eV and 206.4 eV), as well as Nb $3d_{5/2}$ (at 207.1 eV and 203.8 eV), which represents the niobium backbone of the Janus structure. Moreover, Figure 3b shows the deconvoluted XPS peaks corresponding to Se $3p_{3/2}$ (159.8 eV), S $2p_{3/2}$ (160.5 eV), S $2p_{1/2}$ (161.8 eV), and Se $3p_{1/2}$ (166.2 eV), providing further confirmation of the distinct sulfur and selenium contributions. The Se^{2-} $3d_{3/2}$ (53.2 eV and 55.4 eV) and Se^{2-} $3d_{5/2}$ (54.3 eV), shown in Figure 3c, are indicative of Nb-Se bonding formed during SEAR selenization of NbS_2. Additionally, Figure 3d shows the deconvoluted peaks for S 2s and Se 3s orbitals at 228.5 eV and 230.2 eV, respectively. Overall, the spectral deconvolution revealed the distinct chemical contribution from both sulfur and selenium, underscoring the Janus structure containing both types of chalcogen atoms. The stoichiometry ratio was calculated to be S:Nb:Se = 1.09:1.16:1 by using the integrated peak areas of S 2p, Nb 3d, and Se 3p orbitals corrected to their respective relative sensitivity factor (RSF). Details of stoichiometry calculations are provided in the Supplementary Information file.

To understand the mechanism of the degradation process of SNbSe monolayer, observed in Raman Figure 2c and by visual changes in Figure S5, XPS measurements were also performed on a four-day-old sample that had been exposed to the ambient environment. The collected XPS spectra showed oxidation signatures, evident in both Nb 3d and Se 3d spectra (SI Figure S7). That oxidation is presumed to occur predominantly in the topmost Se atomic layer introduced during the SEAR selenization process. This is corroborated by the emergence of a prominent Se-O bonding peak at 59 eV representing SeO_2. Furthermore, the disappearance of the Nb $3d_{5/2}$ (203.8 eV) peak and the redshift of remaining Nb peaks can be related to the formation of Nb-O bonding such as in the case of the Nb_2O_5 or NbO_2 amorphous layer. These findings further support the oxidation behavior of Janus SNbSe under ambient conditions.

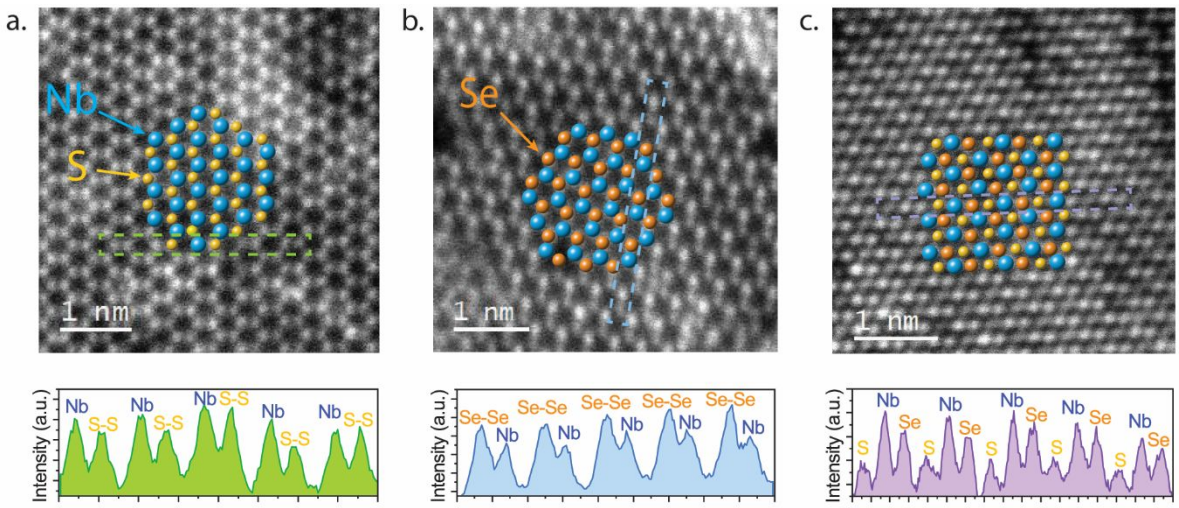

Figure 4. Z-contrast HAADF STEM images of (a) 1H-NbS_2, (b) 1H-$NbSe_2$, and (c) 1T-SeNbS overlaid with color-coded spheres indicating the different atoms. Under each image is the Z intensity of the boxed region for each respective material system. The lattice constant of each material system was determined by measuring the distance between the two nearest neighboring Nb (blue) atoms in each image. The measured lattice constants for 1H-NbS_2, 1H-$NbSe_2$, and 1T-SeNbS are 3.46 ± 0.14 Å, 3.73 ± 0.16 Å, 3.48 ± 0.07 Å, respectively, and are in good agreement with theoretically obtained values of 3.34 Å, 3.47 Å, 3.43 Å.

Direct evidence of 1H-to-1T phase transition

To observe and confirm the 1H to 1T phase transition during the Janus conversion, Z-contrast HAADF STEM was used to capture the changes in the positions of the newly replaced S atoms from $NbSe_2$ to SeNbS. Figure 4a-c shows the Z-contrast HAADF STEM images for 1H-NbS_2, 1H-$NbSe_2$, and 1T-Janus SeNbS (converted from 1H-$NbSe_2$), respectively. Each image is superimposed with a "billiard ball" atomic model to highlight the Nb atoms and corresponding chalcogen positions. A direct comparison between Figure 4b and 4c reveals the transformation from the hollow-centered trigonal prismatic 1H-$NbSe_2$ structure to the filled-centered octahedral 1T-SeNbS Janus structure, providing evidence of the newly incorporated S atoms. The change from hollow-centered to filled-center is an indication of in-plane atomic displacement associated with the 1H-to-1T transition as illustrated in Figure 1a. The intensity histogram under each STEM image displays the relative intensities corresponding to Nb, Se-Se stacking, S-S stacking, Se, and S. In the 1H-$NbSe_2$ phase, the atomic mass of the stacked Se atoms exceeds that of a single Nb atom, resulting in a brighter contrast due to increased electron scattering. In contrast, for 1H-NbS_2, the atomic mass of Nb surpasses that of two sulfur atoms, leading to an inverse contrast. In the case of the 1T-SeNbS phase, in-plane displacement atomic displacement during the phase transition resulted in all three atomic layers being visible along the z-axis with no tilt. The intensity histogram clearly distinguishes each element by its

characteristic electron scattering, reflecting the differential atomic mass and providing further confirmation of the phase transition.

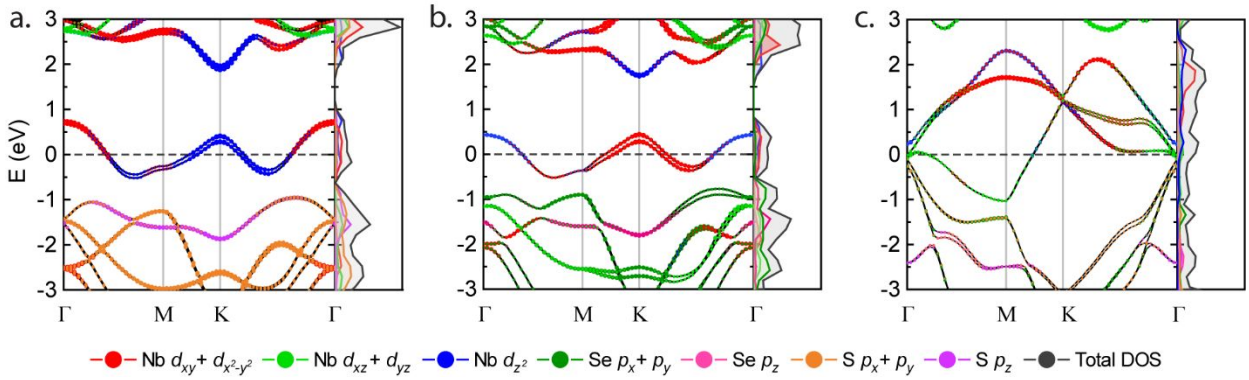

Figure 5. Orbital projected electronic band structure for (a) 1H-NbS_2, (b) 1H-$NbSe_2$, and (c) 1T-NbSSe calculated using DFT. DOS with orbital contribution breakdown is plotted to the right of each plot with the same color coordination.

Theoretical and experimental insights on the electronic properties of metallic Janus SNbSe

DFT calculations were performed using a 2x2x1 supercell with Γ-centered Brillouin zone to calculate both the electronic band structures and phonon dispersions. Figure 5a-c illustrates the GGA+SOC band structures for 1H-NbS_2, 1H-$NbSe_2$, and 1T-SNbSe monolayers, respectively. Notably, the electronic band structure of 1T-SeNbS mirrors that of 1T-SNbSe, owing to the preservation of crystal symmetry, irrespective of chalcogen orientation. Consequently, both SNbSe and SeNbS monolayers share the same space group: P3m1 (156) and point group: C 3v symmetry. Furthermore, the total energy is identical with an accuracy of 10^{-6} eV/atom for these two structures. Therefore, their electronic and vibrational properties will be identical.

Both the parent and the Janus monolayers exhibit metallic behavior, as evidenced by the crossing of the Nb d-bands at the Fermi level (E_F). However, the characteristic band structures of $NbSe_2$ and NbS_2 markedly differ from that of SNbSe. This discrepancy arises from the distinct crystal field environments experienced by the Nb atoms, namely the trigonal prismatic environment in the 1H phase and the octahedral environment in the 1T phase. In the 1H structure, the trigonal prismatic environment induces a splitting of the *d* orbitals, resulting in a lower-lying d_{z^2} singlet followed by a doubly degenerate (d_{xy} + $d_{x^2-y^2}$) and a higher-energy doublet (d_{xz} + d_{yz}). Given the covalent nature of these compounds, a significant admixture of different *d*-orbitals is observed. In both $NbSe_2$ and NbS_2, the band crossing the E_F (Figure 5a-b) is primarily occupied by d_{z^2} orbitals, with a partial mixing of (d_{xy} + $d_{x^2-y^2}$) orbitals. Conversely, due to the octahedral environment of Nb atoms in the 1T structure, the *d* orbitals split into low-energy t_{2g} bands (d_{xy}, d_{xz}, d_{yz}) and high-energy e_g bands ($d_{x^2-y^2}$, d_{z^2}). Consequently, the bands crossing E_F (Figure 5c) reflect orbital occupancy consistent with the crystal field environment of 1H (for NbS_2 and $NbSe_2$) or 1T (for SNbSe) phases. The unique orbital

characteristics in the NbS_2 and $NbSe_2$ electronic band structures, as predicted using DFT, have been experimentally verified using angle-resolve photoemission spectroscopy (ARPES),[57, 58] which employs linearly polarized light to differentiate between in-plane and out-of-plane orbitals components. This approach can also be applied to 1T-SNbSe to enhance our understanding of the orbital contributions to the Janus band structure.

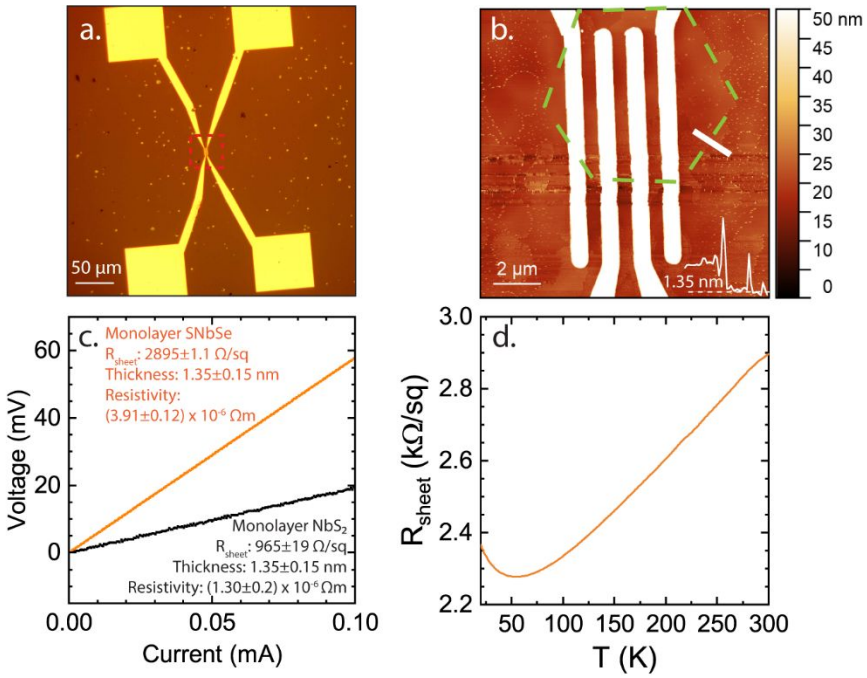

Figure 6. (a) Optical microscope image of the metal contact fabricated using photolithography for four-probe resistance measurement. The red box highlights the position of the SNbSe flake. (b) AFM scan of the metal probes deposited on top of the SNbSe flake, was performed from the region within the red box in (a). (c) I-V measurement of NbS_2 and SNbSe Janus monolayer. (d) SNbSe sheet resistance as a function of temperature from 300 K to 20 K.

To support findings based on the electronic band structure calculations about the metallic behavior of NbS_2 and SNbSe, additional I-V measurements were performed. The main goal of this experiment was to obtain the resistivity of the same monolayer before (for NbS_2) and after SEAR conversion (for SNbSe). For that purpose, the four-probe method was used with metal contacts composed of Ti/Au patterned onto a CVD-grown NbS_2 monolayer via photolithography, as depicted in Figure 6a. An initial four-probe measurement was performed on the pristine NbS_2 as a reference, followed by SEAR conversion to Janus SNbSe, after which a second I-V measurement was conducted. The sheet resistance and sample thickness were determined respectively through I-V sweeps using a semiconductor device parameter analyzer (Keysight B1500A) and AFM (Figure 6b). Subsequently, the resistivity was calculated by the product of sheet resistance and thickness. The results of the four-probe electrical measurement revealed a linear I-V characteristic for both NbS_2 and SNbSe, with current sweeping from 0 to 100 µA (Figure 6c). The obtained resistivity for NbS_2 (1.3×10^{-6} Ωm) is comparable to values obtained in other studies ($1.25–2.5 \times 10^{-6}$ Ωm),[59] where the metallic character of NbS_2 was confirmed based on temperature-dependent resistivity measurements.[59, 60] This conclusion aligns well with the findings of the electronic band structure

calculations revealing metallic behavior through a high density of states at the Fermi level and closed band gap (the crossing of the Nb d-bands at the Fermi level). Similar observations were made in the case of the electronic band structure obtained for the SNbSe monolayer, proving metallic behavior for that sample. However, the resistivity of the SNbSe (3.9×10^{-6} Ωm) increased after conversion from the same monolayer. The higher value of the resistivity for SNbSe can stem from the increased/introduced defects to the parent crystal during the conversion process. Moreover, the sheet resistance of SNbSe was measured as a function of temperature to further confirm the metallic behavior, shown in Figure 6d. It can be seen that the value of the sheet resistance decreases with temperature in the range from 300 to 50 K as expected for metallic electronic transport, followed by an increase of the sheet resistance starting from 50 K. This observed behavior in trend reversal can be related to weak localization and/or onset of Anderson localization, where both possibly originate from defects or impurities in the studied material.

CONCLUSION

Metallic 1T-SNbSe and 1T-SeNbS Janus structures were successfully synthesized from their parent 1H-phase metallic NbS_2 and $NbSe_2$ TMDs, through a controlled selenization and sulfurization process via selective epitaxial atomic replacement (SEAR). The results have demonstrated a structural 1H → 1T phase transition during the Janus conversion, corroborated by indirect phononic signatures and direct atomic-scale imaging. Comprehensive theoretical and experimental analyses confirm the retention of metallic behavior in the SNbSe Janus structure. Nevertheless, further investigations are necessary to enhance crystalline quality and to elucidate their electronic properties, potentially towards the demonstration of 2D Anderson-Blaunt polar metals. These findings represent the pioneering effort in stabilizing Nb-based Janus metals, expanding the library of Janus materials towards their metallic counterparts, and opening new avenues for advanced applications in low-dimensional quantum materials.

EXPERIMENTAL METHODS

APCVD growth of monolayer NbS_2. Monolayer 1H-NbS_2 is grown on pre-cleaned *c*-cut single-side-polish sapphire substrate using a single-zone 1-inch tube furnace APCVD setup. 10 mg of Nb_2O_5 (Sigma-Aldrige) was mixed with 1 mg of NaCl (Sigma-Aldrige) as the niobium precursor, and crystalized sulfur pallets (Sigma-Aldridge) were placed 17 cm upstream as the sulfur precursor. The growth begins with a 40-minute ramp from room temperature to 850 ˚C under a steady flow of 120 sccm Ar carrier gas. Once the temperature reaches 850 ˚C, the H_2 gas flow is turned on at 12 sccm. The furnace is then held at 850 ˚C for 20 minutes for the NbS_2 growth, followed by a slow cool to 650 ˚C (furnace lid half open) and then quenched to room temperature (furnace lid fully open).

Mechanical Exfoliation of monolayer $NbSe_2$. Chemical vapor transport (CVT) grown bulk 2H-$NbSe_2$ crystals were grown and used as the starting materials for mechanical exfoliation down to 1H-$NbSe_2$. A large and relatively flat crystal is preferred as the starting material for exfoliation. Scotch tape is used to repeatedly exfoliate the 2H-$NbSe_2$ crystal down to thin layers, followed by stamping the thin layers to an X4 PDMS film (GEL-PAK). The thin layers are again transferred to O_2 plasma-cleaned Si/SiO_2 (300 nm) substrates by stamping; this final transfer step thins down the layers one last time. Optical microscopy is

used to locate the 1H-$NbSe_2$ monolayers on the substrates. The samples with monolayer $NbSe_2$ are subjected to ultrahigh vacuum (10^{-7} Torr) annealing at 300 ˚C for one hour to remove the gap between the monolayer and the substrate.

SEAR Janus Conversion of SNbSe and SeNbS. The SEAR Janus conversion of SNbSe from NbS_2 took place inside a 1-inch quartz tube, as shown in Figure 1h with monolayer NbS_2 placed in the center. A copper coil is wrapped around the tube and connected to a 13.56 MHz RF power supply for inductively coupled plasma (ICP) generation. The monolayer sample is placed 2 cm upstream from the coil, and a crystallized selenium source is placed 17 cm upstream from the coil. The position of the sample and chalcogen source is based on the plasma length, which depends on the RF power and chamber pressure. The conversion process begins with pumping down the quartz tube to 10 mTorr base pressure, followed by purging with 25 sccm of H_2 for 10 minutes. RF power is set to 90 W and held for 600 seconds of conversion time. The SEAR Janus conversion of SeNbS is similar to that of SNbSe but in a different quartz chamber geometry; it is the same as the one reported in Ref. 11[11]. The sample is placed 6 cm upstream from the copper coil, and a crystallized sulfur source is placed 9 cm upstream from the coil. The plasma conversion process is carried out under 5W of RF power and 3.3 sccm of H_2 flow for 600 seconds.

Raman spectroscopy Measurement. Raman measurements were taken on the Renishaw InVia Raman Spectrometer with an excitation wavelength of 488 nm blue laser. The laser power is controlled to ~100 μW to minimize sample damage. A 2400/mm grating and a 100x microscope objective were used. Raman signal collection occurs over 20 seconds with 1 accumulation at room temperature and ambient pressure.

X-ray Photoelectron Spectroscopy Measurement. X-ray photoelectron spectroscopy (XPS) measurements of CVD NbS_2 converted SNbSe were taken on the Kratos Axis Supra + to confirm the elemental compositions. The XPS is equipped with a dual monochromatic Al K-alpha (1486 eV)/Ag L-alpha (2984.2 eV) x-ray source. The measurement of SNbSe was taken over a 200 μm^2 area with 1 μm ultimate spatial resolution. The XPS is operated in an ultrahigh vacuum environment at ~10^{-9} Torr. The samples were grown and converted on an Al_2O_3 substrate and mounted to a sample holder with a screw-on metal clip. The peak fitting and analysis were done using CasaXPS software; Gaussian/Lorentzian fitting was used for fitting peak shapes.

Scanning Transmission Electron Microscopy. Sample preparation. Monolayer $NbSe_2$ and monolayer SeNbS on Si/SiO_2 were transferred onto the Quantifoil holey carbon grid using a dry transfer technique. The process begins with spin coating the sample with a 5 wt% solution of poly (bisphenol A carbonate) (PC) dissolved in amine-stabilized chloroform. The polymeric thin films were dried on a hot plate at 100 ˚ C, forming a uniform film. The TMD/PC assembly was transferred using adhesive thermal release tape (Nitto Denko REVALPHA, TRT). This assembly was carefully placed onto a Quantifoil holey carbon grid using micromanipulators. A glass slide was used to facilitate handling and heating to 150˚C, allowing the separation of the TMD/PC structure from the TRT. The PC film was dissolved in chloroform and subsequently dried in an oven. The final transferred monolayers were inspected under a microscope and through Raman spectroscopy to confirm the absence of chloroform residue. **STEM.** The scanning

transmission electron microscopy images were collected on a Nion Hermes Ultra STEM 100 microscope operated at 100 keV acceleration voltage, the probe convergence angle was set to 34 mrad, a beam current on the detector was about 50 pA, and an inner collection semi-angle of 80 mrad on the annular detector. The sample was baked at 160˚ C for 8 hours in a UHV environment before the experiment. The images are filtered and denoised by deconvolution of the point spread function of the electron beam from the raw image by the Richardson-Lucy deconvolution algorithm.

DFT Calculations

Density functional theory (DFT) calculations have been performed using a plane-wave basis set with a kinetic energy cutoff of 450 eV and projector augmented-wave potentials[61], as implemented in the Vienna Ab initio Simulation Package (VASP)[62]. The Perdew-Burke-Ernzerhof (PBE)[63] version of the generalized gradient approximation (GGA) has been employed as the exchange-correlation functional. In order to construct monolayers, a vacuum of 18 Å along the (001) direction was introduced. Both in-plane lattice constants and atomic positions were relaxed using GGA until the total energy converged to 10−8 eV, and the forces on each atom converged to 0.001 eV/Å. Furthermore, spin-orbit coupling (SOC) was included in our calculations to get the correct electronic band dispersion for NbS2, NbSe2, and Janus SNbSe monolayers. Reciprocal space integration was carried out using a Γ-centered k-mesh of 24×24×1. Phonon dispersions were calculated using density functional perturbation theory (DFPT)[64] as implemented in the PHONOPY code[65] using a 2×2×1 supercell of the respective monolayers and a 12×12×1 k-mesh.

Electrical Contact Patterning on NbS_2

Four metal electrodes on top of the flakes were fabricated using standard lithography and metal deposition techniques. Each metal electrode consists of a 70 x 70 μm contact pad with a 700 nm wide finger extending to the NbS_2 flake, with an inter-finger spacing of 700 nm. First, bilayer photoresists were spin-coated onto the sapphire substrates containing CVD-grown monolayer NbS_2 flakes (LOR3A: 4000 rpm, 30s; 180 °C, 2min; AZ3312: 4000 rpm, 30s; 100°C, 1 min). The photoresist layers were exposed using a maskless aligner (MLA 150), followed by a post-exposure bake at 110 °C for 1 min. The exposed photoresists were developed using AZ MIF300 for 1 minute and thoroughly rinsed with DI water. Subsequently, the substrates with the patterned photoresists were loaded into an e-beam metal deposition chamber (Kurt J. Lesker Company) for the deposition of 5 nm of Ti and 80 nm of Au under a deposition pressure of ~5e-7 Torr and deposition rates of 0.5A/s for both Ti and Au. The fabrication process was completed by lifting off the metal layers on top of the photoresists using PG Remover at 100 °C, followed by thoroughly rinsing the sapphire substrates with DI water.

Four-Probe Measurement

Electrical resistance was measured using the four-probe technique using a semiconductor device parameter analyzer (Keysight B1500A). A current sweep was performed on the outer two electrodes from 0 to 100 μA while the inner two electrodes measured the voltage, and sheet resistance was calculated from the measured current-voltage curve with measured thickness. NbS_2 was first measured after the electrode patterning process, followed by SEAR conversion of NbS_2 to SNbSe, and finally, the same sample was

measured again. Temperature-dependent resistance measurement of SNbSe was carried out using PPMS (Quantum Design) on the same structure.

AUTHOR CONTRIBUTIONS

Cheng-Lun Wu – Conceptualization, Formal analysis, Investigation, Writing – original draft (lead).
Mohammad Y. Sayyad – Formal analysis, Investigation, Writing – original draft (supporting).
Renee E. Sailus – Investigation, Formal analysis, Validation.
Dibyendu Dey – Formal analysis, Investigation, Writing – original draft (supporting).
Jing Xie – Methodology, Formal analysis, Investigation.
Patrick Hayes – Validation.
Jan Kopaczek – Formal analysis, Writing – review & editing.
Yunbo Ou – Formal analysis, Investigation.
Sandhya Susarla – Project administration.
Ivan S. Esqueda – Project administration.
Antia S. Botana – Project administration.
Seth A. Tongay – Conceptualization, Funding acquisition, Supervision, Writing – review & editing.

CONFLICT OF INTEREST

There are no conflicts to declare.

DATA AVAILABILITY

The data supporting this article have been included as part of the Supplementary Information.

ACKNOWLEDGMENT

S.T acknowledges primary support from DOE-SC0020653 (materials synthesis), Arizona State University STC funds, DMR 2111812 (manufacturing), DMR 2206987 (vibrational studies), and CMMI 2129412 (scaling). Partial funding is provided by the Arizona Water Innovation Initiative Global Center for Water Technology. S.T. also acknowledges partial support from Lawrence Semiconductor Labs. We acknowledge the use of facilities within the Eyring Materials Center at Arizona State University.

REFERENCES

(1) Zheng, T.; Y.C. Lin; Y. Yu; P. Valencia-Acuna; A.A. Puretzky; R. Torsi; C. Liu; I.N. Ivanov; G. Duscher; D.B. Geohegan; Z. Ni; K. XiaoH. Zhao, Excitonic Dynamics in Janus MoSSe and WSSe Monolayers. *Nano Lett*, 2021. 21(2): p. 931-937.
(2) Chen, J.; K. Wu; H. Ma; W. HuJ. Yang, Tunable Rashba spin splitting in Janus transition-metal dichalcogenide monolayers via charge doping. *RSC Adv*, 2020. 10(11): p. 6388-6394.

(3) Cheng, Y.C.; Z.Y. Zhu; M. TahirU. Schwingenschlögl, Spin-orbit–induced spin splittings in polar transition metal dichalcogenide monolayers. *EPL (Europhysics Letters)*, 2013. 102(5).
(4) Hu, T.; F. Jia; G. Zhao; J. Wu; A. StroppaW. Ren, Intrinsic and anisotropic Rashba spin splitting in Janus transition-metal dichalcogenide monolayers. *Physical Review B*, 2018. 97(23).
(5) Lu, A.Y.; H. Zhu; J. Xiao; C.P. Chuu; Y. Han; M.H. Chiu; C.C. Cheng; C.W. Yang; K.H. Wei; Y. Yang; Y. Wang; D. Sokaras; D. Nordlund; P. Yang; D.A. Muller; M.Y. Chou; X. ZhangL.J. Li, Janus monolayers of transition metal dichalcogenides. *Nat Nanotechnol*, 2017. 12(8): p. 744-749.
(6) Li, F.; W. Wei; H. Wang; B. Huang; Y. DaiT. Jacob, Intrinsic Electric Field-Induced Properties in Janus MoSSe van der Waals Structures. *J Phys Chem Lett*, 2019. 10(3): p. 559-565.
(7) Liang, J.; W. Wang; H. Du; A. Hallal; K. Garcia; M. Chshiev; A. FertH. Yang, Very large Dzyaloshinskii-Moriya interaction in two-dimensional Janus manganese dichalcogenides and its application to realize skyrmion states. *Physical Review B*, 2020. 101(18).
(8) Yuan, J.; Y. Yang; Y. Cai; Y. Wu; Y. Chen; X. YanL. Shen, Intrinsic skyrmions in monolayer Janus magnets. *Physical Review B*, 2020. 101(9).
(9) Du, W.; K. Dou; Z. He; Y. Dai; B. HuangY. Ma, Spontaneous Magnetic Skyrmions in Single-Layer CrInX(3) (X = Te, Se). *Nano Lett*, 2022. 22(8): p. 3440-3446.
(10) Maghirang, A.B.; Z.-Q. Huang; R.A.B. Villaos; C.-H. Hsu; L.-Y. Feng; E. Florido; H. Lin; A. BansilF.-C. Chuang, Predicting two-dimensional topological phases in Janus materials by substitutional doping in transition metal dichalcogenide monolayers. *npj 2D Materials and Applications*, 2019. 3(1).
(11) Qin, Y.; M. Sayyad; A.R. Montblanch; M.S.G. Feuer; D. Dey; M. Blei; R. Sailus; D.M. Kara; Y. Shen; S. Yang; A.S. Botana; M. AtatureS. Tongay, Reaching the Excitonic Limit in 2D Janus Monolayers by In Situ Deterministic Growth. *Adv Mater*, 2022. 34(6): p. e2106222.
(12) Trivedi, D.B.; G. Turgut; Y. Qin; M.Y. Sayyad; D. Hajra; M. Howell; L. Liu; S. Yang; N.H. Patoary; H. Li; M.M. Petric; M. Meyer; M. Kremser; M. Barbone; G. Soavi; A.V. Stier; K. Muller; S. Yang; I.S. Esqueda; H. Zhuang; J.J. FinleyS. Tongay, Room-Temperature Synthesis of 2D Janus Crystals and their Heterostructures. *Adv Mater*, 2020. 32(50): p. e2006320.
(13) Petrić, M.M.; M. Kremser; M. Barbone; Y. Qin; Y. Sayyad; Y. Shen; S. Tongay; J.J. Finley; A.R. Botello-MéndezK. Müller, Raman spectrum of Janus transition metal dichalcogenide monolayers WSSe and MoSSe. *Physical Review B*, 2021. 103(3).
(14) Zheng, T.; Y.C. Lin; N. Rafizadeh; D.B. Geohegan; Z. Ni; K. XiaoH. Zhao, Janus Monolayers for Ultrafast and Directional Charge Transfer in Transition Metal Dichalcogenide Heterostructures. *ACS Nano*, 2022. 16(3): p. 4197-4205.

(15) Li, H.; Y. Qin; B. Ko; D.B. Trivedi; D. Hajra; M.Y. Sayyad; L. Liu; S.H. Shim; H. ZhuangS. Tongay, Anomalous Behavior of 2D Janus Excitonic Layers under Extreme Pressures. *Adv Mater*, **2020**. 32(33): p. e2002401.
(16) Lin, Y.C.; C. Liu; Y. Yu; E. Zarkadoula; M. Yoon; A.A. Puretzky; L. Liang; X. Kong; Y. Gu; A. Strasser; H.M. Meyer, 3rd; M. Lorenz; M.F. Chisholm; I.N. Ivanov; C.M. Rouleau; G. Duscher; K. XiaoD.B. Geohegan, Low Energy Implantation into Transition-Metal Dichalcogenide Monolayers to Form Janus Structures. *ACS Nano*, **2020**. 14(4): p. 3896-3906.
(17) Yagmurcukardes, M.; Y. Qin; S. Ozen; M. Sayyad; F.M. Peeters; S. TongayH. Sahin, Quantum properties and applications of 2D Janus crystals and their superlattices. *Applied Physics Reviews*, **2020**. 7(1).
(18) Zhang, J.; S. Jia; I. Kholmanov; L. Dong; D. Er; W. Chen; H. Guo; Z. Jin; V.B. Shenoy; L. ShiJ. Lou, Janus Monolayer Transition-Metal Dichalcogenides. *ACS Nano*, **2017**. 11(8): p. 8192-8198.
(19) Liu, Y.T. Gao, First-principles study of controllable contact types in Janus MoSH/GaN van der Waals heterostructure. *J Chem Phys*, **2023**. 159(9).
(20) Wang, J.; L. Bai; X. Zhao; C. ChenL. Niu, Controllable contact types of Janus MoSH and WSi2N4 van der Waals heterostructures via biaxial strain and external electric field. *Physica E: Low-dimensional Systems and Nanostructures*, **2023**. 149.
(21) Ahmed, D.; N. MuhammadZ.J. Ding, Metallic CoSb and Janus Co(2)AsSb monolayers as promising anode materials for metal-ion batteries. *Phys Chem Chem Phys*, **2024**. 26(24): p. 17191-17204.
(22) Li, T.-K.; X.-J. Ye; X.-H. Zheng; R. JiaC.-S. Liu, Theoretical Prediction of Janus TQ-Graphene as a Metallic Two-Dimensional Carbon Allotrope with Negative Poisson's Ratios for High Capacity Sodium-Ion Batteries. *ACS Applied Nano Materials*, **2023**. 6(14): p. 13188-13195.
(23) Fu, Y.; Y. Shan; G. Zhou; L. Long; L. Wang; K. Yin; J. Guo; J. Shen; L. LiuX. Wu, Electric Strain in Dual Metal Janus Nanosheets Induces Structural Phase Transition for Efficient Hydrogen Evolution. *Joule*, **2019**. 3(12): p. 2955-2967.
(24) Bai, Y.; R. Guan; H. Zhang; Q. ZhangN. Xu, Efficient charge separation and visible-light response of two-dimensional Janus group-III monochalcogenide multilayers. *Catalysis Science & Technology*, **2021**. 11(2): p. 542-555.
(25) Anderson, P.W.E.I. Blount, Symmetry Considerations on Martensitic Transformations: "Ferroelectric" Metals? *Physical Review Letters*, **1965**. 14(7): p. 217-219.
(26) Zheludev, I.S., *Ferroelectricity and Symmetry*. 1971. p. 429-464.
(27) Fei, Z.; W. Zhao; T.A. Palomaki; B. Sun; M.K. Miller; Z. Zhao; J. Yan; X. XuD.H. Cobden, Ferroelectric switching of a two-dimensional metal. *Nature*, **2018**. 560(7718): p. 336-339.
(28) Yang, Q.; M. WuJ. Li, Origin of Two-Dimensional Vertical Ferroelectricity in WTe(2) Bilayer and Multilayer. *J Phys Chem Lett*, **2018**. 9(24): p. 7160-7164.

(29) Liu, X.; Y. Yang; T. Hu; G. Zhao; C. ChenW. Ren, Vertical ferroelectric switching by in-plane sliding of two-dimensional bilayer WTe(2). *Nanoscale*, **2019**. 11(40): p. 18575-18581.
(30) Sharma, P.; F.X. Xiang; D.F. Shao; D. Zhang; E.Y. Tsymbal; A.R. HamiltonJ. Seidel, A room-temperature ferroelectric semimetal. *Science Advances*, **2019**. 5(7).
(31) Falahati, K.; A. KhatibiB. Shokri, Light-matter interaction in tungsten Sulfide-based Janus monolayers: A First-Principles study. *Applied Surface Science*, **2022**. 599.
(32) Kim, S., Construction of optimized tight-binding models usingab initioHamiltonian: application to monolayer 2H-transition metal dichalcogenides. *J Phys Condens Matter*, **2023**. 35(41).
(33) Lucking, M.C.; K. BeachH. Terrones, Large second harmonic generation in alloyed TMDs and boron nitride nanostructures. *Sci Rep*, **2018**. 8(1): p. 10118.
(34) Bölle, F.T.; A.E.G. Mikkelsen; K.S. Thygesen; T. VeggeI.E. Castelli, Structural and chemical mechanisms governing stability of inorganic Janus nanotubes. *npj Computational Materials*, **2021**. 7(1).
(35) Huang, Z.; J.M.P. Aguilar; S. Zeng; Y. TuZ. Gu, Stable Janus monolayer MoSHx ($0.5 \leq x \leq 2$). *Applied Physics Letters*, **2023**. 123(12).
(36) Liu, P.-F.; F. Zheng; J. Li; J.-G. Si; L. Wei; J. ZhangB.-T. Wang, Two-gap superconductivity in a Janus MoSH monolayer. *Physical Review B*, **2022**. 105(24).
(37) Wan, X.; E. Chen; J. Yao; M. Gao; X. Miao; S. Wang; Y. Gu; S. Xiao; R. Zhan; K. Chen; Z. Chen; X. Zeng; X. GuJ. Xu, Synthesis and Characterization of Metallic Janus MoSH Monolayer. *ACS Nano*, **2021**. 15(12): p. 20319-20331.
(38) Wu, Y.-L.; Z.-Y. Zeng; H.-Y. GengX.-R. Chen, Electronic structures and magnetic properties of Janus NbSSe monolayer controlled by carrier doping. *Journal of Applied Physics*, **2024**. 136(9).
(39) Yang, X.; L. Lin; X. GuoS. Zhang, Design of Multifunctional Electrocatalysts for ORR/OER/HER/HOR: Janus Makes Difference. *Small*, **2024**: p. e2404000.
(40) Xiong, F.Y. Chen, A first-principles study of Janus monolayer TiSSe and VSSe as anode materials in alkali metal ion batteries. *Nanotechnology*, **2021**. 32(2): p. 025702.
(41) Mogulkoc, A.; Y. Mogulkoc; S. JahangirovE. Durgun, Characterization and Stability of Janus TiXY (X/Y = S, Se, and Te) Monolayers. *The Journal of Physical Chemistry C*, **2019**. 123(49): p. 29922-29931.
(42) Zhou, L.-F.; X.-W. Gao; T. Du; H. Gong; L.-Y. LiuW.-B. Luo, Two-dimensional NbSSe as anode material for low-temperature sodium-ion batteries. *Chemical Engineering Journal*, **2022**. 435.
(43) Zhou, J.; J. Lin; X. Huang; Y. Zhou; Y. Chen; J. Xia; H. Wang; Y. Xie; H. Yu; J. Lei; D. Wu; F. Liu; Q. Fu; Q. Zeng; C.H. Hsu; C. Yang; L. Lu; T. Yu; Z. Shen; H. Lin; B.I. Yakobson; Q. Liu; K. Suenaga; G. LiuZ. Liu, A library of atomically thin metal chalcogenides. *Nature*, **2018**. 556(7701): p. 355-359.

(44) Li, Z.; W. Yang; Y. Losovyj; J. Chen; E. Xu; H. Liu; M. Werbianskyj; H.A. Fertig; X. YeS. Zhang, Large-size niobium disulfide nanoflakes down to bilayers grown by sulfurization. *Nano Research*, **2018**. 11(11): p. 5978-5988.

(45) Li, Z.; X. Xi; B. Ding; H. Li; E. Liu; Y. YaoW. Wang, Thermodynamics and Kinetics Synergy for Controlled Synthesis of 2D van der Waals Single-Crystal NbSe2 via Modified Chemical Vapor Transport. *Crystal Growth & Design*, **2019**. 20(2): p. 706-712.

(46) Castellanos-Gomez, A.; M. Buscema; R. Molenaar; V. Singh; L. Janssen; H.S.J. van der ZantG.A. Steele, Deterministic transfer of two-dimensional materials by all-dry viscoelastic stamping. *2D Materials*, **2014**. 1(1).

(47) Wang, H.; X. Huang; J. Lin; J. Cui; Y. Chen; C. Zhu; F. Liu; Q. Zeng; J. Zhou; P. Yu; X. Wang; H. He; S.H. Tsang; W. Gao; K. Suenaga; F. Ma; C. Yang; L. Lu; T. Yu; E.H.T. Teo; G. LiuZ. Liu, High-quality monolayer superconductor NbSe(2) grown by chemical vapour deposition. *Nat Commun*, **2017**. 8(1): p. 394.

(48) Lv, Q.; X. QinR. Lv, Controllable Growth of Few-Layer Niobium Disulfide by Atmospheric Pressure Chemical Vapor Deposition for Molecular Sensing. *Frontiers in Materials*, **2019**. 6.

(49) Hill, H.M.; A.F. Rigosi; S. Krylyuk; J. Tian; N.V. Nguyen; A.V. Davydov; D.B. NewellA.R.H. Walker, Comprehensive optical characterization of atomically thin NbSe(2). *Phys Rev B*, **2018**. 98.

(50) Zhao, S.; T. Hotta; T. Koretsune; K. Watanabe; T. Taniguchi; K. Sugawara; T. Takahashi; H. ShinoharaR. Kitaura, Two-dimensional metallic NbS_2: growth, optical identification and transport properties. *2D Materials*, **2016**. 3(2).

(51) Xi, X.; L. Zhao; Z. Wang; H. Berger; L. Forro; J. ShanK.F. Mak, Strongly enhanced charge-density-wave order in monolyaer NbSe2. *Nature Nanotechnology*, **2015**. 10: p. 765-769.

(52) Suzuki, H.; Y. Liu; M. Misawa; C. Nakano; Y. Wang; R. Nakano; K. Ishimura; K. TsurutaY. Hayashi, Intermediate State between MoSe(2) and Janus MoSeS during Atomic Substitution Process. *Nano Lett*, **2023**. 23(10): p. 4533-4540.

(53) Zhang, K.; Y. Guo; Q. Ji; A.Y. Lu; C. Su; H. Wang; A.A. Puretzky; D.B. Geohegan; X. Qian; S. Fang; E. Kaxiras; J. KongS. Huang, Enhancement of van der Waals Interlayer Coupling through Polar Janus MoSSe. *J Am Chem Soc*, **2020**. 142(41): p. 17499-17507.

(54) Zhu, J.; Z. Wang; H. Yu; N. Li; J. Zhang; J. Meng; M. Liao; J. Zhao; X. Lu; L. Du; R. Yang; D. Shi; Y. JiangG. Zhang, Argon Plasma Induced Phase Transition in Monolayer MoS(2). *J Am Chem Soc*, **2017**. 139(30): p. 10216-10219.

(55) Nan, H.; J. Jiang; S. Xiao; Z. Chen; Z. Luo; L. Zhang; X. Zhang; H. Qi; X. Gu; X. WangZ. Ni, Soft hydrogen plasma induced phase transition in monolayer and few-layer MoTe(2). *Nanotechnology*, **2019**. 30(3): p. 034004.

(56) Holler, J.; L. Bauriedl; T. Korn; A. Seitz; F. Özyigit; M. Eichinger; C. Schüller; K. Watanabe; T. Taniguchi; C. StrunkN. Paradiso, Air tightness of hBN encapsulation and its impact on Raman spectroscopy of van der Waals materials. *2D Materials*, **2019**. 7(1).

(57) Nakata, Y.; K. Sugawara; S. Ichinokura; Y. Okada; T. Hitosugi; T. Koretsune; K. Ueno; S. Hasegawa; T. TakahashiT. Sato, Anisotropic band splitting in monolayer NbSe2: implications for superconductivity and charge density wave. *npj 2D Materials and Applications*, 2018. 2(1).

(58) Huang, D.; H. Nakamura; K. Küster; U. Wedig; N.B.M. Schröter; V.N. Strocov; U. StarkeH. Takagi, Probing the interlayer coupling in 2H−NbS2 via soft x-ray angle-resolved photoemission spectroscopy. *Physical Review B*, 2022. 105(24).

(59) Wang, X.; J. Lin; Y. Zhu; C. Luo; K. Suenaga; C. CaiL. Xie, Chemical vapor deposition of trigonal prismatic NbS(2) monolayers and 3R-polytype few-layers. *Nanoscale*, 2017. 9(43): p. 16607-16611.

(60) Song, X.; Y. Wang; F. Zhao; Q. Li; H.Q. Ta; M.H. Rummeli; C.G. Tully; Z. Li; W.J. Yin; L. Yang; K.B. Lee; J. Yang; I. Bozkurt; S. Liu; W. ZhangM. Chhowalla, Plasmon-Free Surface-Enhanced Raman Spectroscopy Using Metallic 2D Materials. *ACS Nano*, 2019. 13(7): p. 8312-8319.

(61) Blochl, P.E., Projector augmented-wave method. *Phys Rev B Condens Matter*, 1994. 50(24): p. 17953-17979.

(62) Kresse, G.J. Furthmuller, Efficient iterative schemes for ab initio total-energy calculations using a plane-wave basis set. *Physical Review B*, 1996. 54(16): p. 11169-11184.

(63) Perdew, J.P.; K. BurkeM. Ernzerhof, Generalized Gradient Approximation Made Simple. *Physical Review Letters*, 1996. 77(18): p. 3865--3868.

(64) Baroni, S.; S.d. Gironocoli; A.D. CorsoP. Giannozzi, Phonons and related crystal properties from density-functional perturbation theory. *Reviews of Modern Physics*, 2001. 73(2): p. 515-562.

(65) Togo, A.I. Tanaka, First principles phonon calculations in materials science. *Scripta Materialia*, 2015. 108: p. 1-5.

DATA AVAILABILITY

The data supporting this article have been included as part of the Supplementary Information.